Manganese deception on graphene and implications in catalysis

Ruquan Ye[†], **Juncai Dong**[‖], **Luqing Wang**[§], **Rubén Mendoza-Cruz**[#], **Yilun Li**[†], **Peng-Fei An**[‖], **Miguel José Yacamán**[#,*], **Boris I. Yakobson**[†,‡,*], **Dongliang Chen**[‖,*], and **James M. Tour**[†,‡,§,*]

[†]Department of Chemistry, Rice University, 6100 Main Street, Houston, Texas 77005, USA

[‡]Smalley-Curl Institute and the NanoCarbon Center, Rice University, 6100 Main Street, Houston, Texas 77005, USA

[§]Department of Materials Science and NanoEngineering, Rice University, 6100 Main Street, Houston, Texas 77005, USA

[‖]Beijing Synchrotron Radiation Facility, Institute of High Energy Physics, Chinese Academy of Sciences, Beijing 100049, China

[#]Department of Physics and Astronomy, University of Texas at San Antonio, One UTSA Circle, San Antonio, Texas 78249, USA

Abstract

Heteroatom-doped metal-free graphene has been widely studied as the catalyst for the oxygen reduction reaction (ORR). Depending on the preparation method and the dopants, the ORR activity varies ranging from a two-electron to a four-electron pathway. The different literature reports are difficult to correlate due to the large variances. However, due to the potential metal contamination, the origin of the ORR activity from "metal-free" graphene remains confusing and inconclusive. Here we decipher the ORR catalytic activities of diverse architectures on graphene derived from reduced graphene oxide. High angle annular dark field scanning transmission electron microscopy, X-ray absorption near edge structure, extended X-ray absorption fine structure, and trace elemental analysis methods are employed. The mechanistic origin of ORR activity is associated with the trace manganese content and reaches its highest performance at an onset potential of 0.94 V when manganese exists as a mononuclear-centered structure within defective graphene. This study exposes the deceptive role of trace metal in formerly thought to be metal-free graphene materials. It also provides insight into the design of better-performing catalyst for ORR by underscoring the coordination chemistry possible for future single-atom catalyst materials.

Supplementary Data. Supplementary data can be found at:

Competing financial interests
The authors declare no competing financial interests.

TOC image
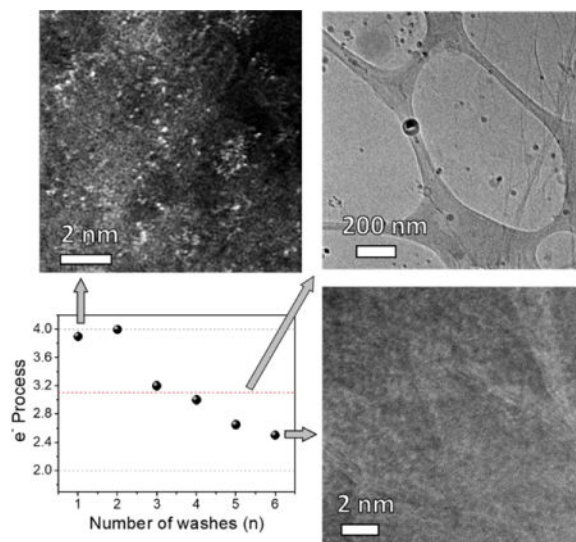
Keywords

metal-free catalyst; oxygen reduction reaction; heteroatom-doped graphene; metal-free graphene

1. Introduction

Graphene and its hybrid materials have been shown to have much utility across a diversity of fields including membranes [1–2], electronics [3] and catalysis [4–5] due to its excellent chemical, mechanical and electronic properties [6–8]. In particular, heteroatom-doped metal-free graphene a candidate as a catalyst in ORR fuel cells due to its performance being comparable to that of scarce platinum [9–12]. Numerous studies have been conducted to improve its catalytic activity from a two-electron to a four-electron oxygen reduction process [9–10,13–15]. However, the designation of "metal-free" has been controversial due to the potential contamination of metals from the precursor, reactant or reaction vessels [14,16]. For example, encapsulated trace iron within carbon nanotubes enhanced the catalytic activity, and removal of iron results in an inferior performing material [14]. By using more sensitive analytical techniques such as electron paramagnetic resonance (EPR) and inductively coupled plasma mass spectrometry (ICP-MS), researchers have successfully detected manganese signals in reduced graphene oxide (rGO) synthesized using Hummer's method [17–18]. The trace metals are difficult to remove and are below the detection limits of common tools such as X-ray diffraction (XRD) and X-ray photoelectron spectroscopy (XPS) [19–21]. These trace metal impurities are introduced to the catalyst from the graphite precursor or reactants that have been used to make the catalyst. Trace metals have been found to affect the electrochemical performance of graphene [17,22]. It has been suspected that the ORR activity of graphene comes from MnO_2 particles in light of the fact that contaminated graphene or MnO_2 have better performance than other metal oxides and metal-free graphitic materials [17].

Single-atom catalysis is a recent advance that has attained broad research interests in various catalytic systems. In these studies, the mononuclear distributed atoms on graphene or other matrixes not only possess higher atomic economy, but also exhibit higher catalytic activities than nanoparticles comprised of the same metal [23–26]. This inspired us to revisit the role of trace metal in the electrochemical performance of graphene. In this work, we synthesized graphene-based materials with different structures and their ORR catalytic activities were determined. This includes nitrogen-doped graphene (NG), NG containing manganese oxide nanoparticles and Mn mononuclear-centered architectures within graphene. Using a combination of analytical tools including high angle annular dark field scanning transmission electron microscopy (HAADF-STEM), X-ray absorption near edge structure (XANES) and extended X-ray absorption fine structure (EXAFS), the manganese-centered structures within the defective graphene are studied. Those trace metal-containing materials were highly active in reducing O_2 into OH^- through a four-electron process. The work permits the rationalization of an otherwise convoluted literature on the topic of "metal-free" electrocatalysis on graphene. While the research on "metal-free" graphene catalysis continues to increase, the role of trace metals in other systems remains to be further investigated in light of the divergent results in the literature [27–28]. These results will be of significance for the engineering of higher-performing ORR catalysts, and could have important implications in future development of graphene-based catalysts for other reaction systems.

2. Experimental

2.1. Synthesis of GOn

GOn were synthesized using the improved Hummers method [29]. To a 9:1 mixture of concentrated H_2SO_4/H_3PO_4 (720:80 mL) was added a mixture of graphite flakes (6.0 g, 1 wt equiv Sigma-Aldrich 332461). $KMnO_4$ (36.0 g, 6 wt equiv) was slowly added in 6 equal portions, producing a slight exotherm to 35 – 40°C. The reaction was then heated to 50°C and stirred for 12 h. *Do not concentrate this solution since concentrated $KMnO_4$ in acid can be explosive* [29]. The reaction was cooled to r.t. and poured onto ice (~ 800 mL) with 30% H_2O_2 (6 mL). For workup, the mixture was centrifuged (4000 rpm for 4 h) and the supernatant was decanted away. The remaining solid material was then divided into 6 portions. Each portion was washed in succession with 200 mL of 30% HCl (n×, n = 1 – 6), then 200 mL of water, and finally 200 mL of ethanol (2×). For each wash, the mixture was centrifuged at 4000 rpm for 4 h and the supernatant was decanted away. The material remaining after this extended multiple-wash process was coagulated with 200 mL of ether, and the resulting suspension was filtered over a PTFE membrane with a 0.45 μm pore size. The solid obtained on the filter was vacuum-dried overnight at room temperature.

2.2. Synthesis of NGn

GOn (30 mg) was added into HPLC grade water (15 mL) and sonicated (Cole Parmer, model 08849-00) for 12 h. The solution was then transferred into a Teflon-sealed autoclave and heated at 160°C for 12 h. To avoid contamination, the Teflon cell was soaked in 98% H_2SO_4 for 1 h and washed with HPLC grade water between each experiment. After cooling to r.t., the water was decanted away and the aerogel was rinsed with 15 mL HPLC grade water

(2×). The remaining aerogel was freeze-dried by cooling in liquid nitrogen and then sublimating the water under vacuum. Nitrogen doping was performed in a CVD furnace. Typically, the aerogel was placed in a 1-in (2.54 cm) quartz tube. The quartz tube was evacuated to ~ 100 mTorr and filled with Ar/NH_3 (65:65 sccm) to 1 atm. After that, the temperature of the furnace was raised to 750°C within 30 min and maintained at 750°C for 1 h under contineous Ar/NH_3 flow (65:65 sccm). The nitrogen-doping process results in a ~30% wt loss due to the etching effect of NH_3.

2.3. Synthesis of NG1a

To HPLC grade water (15 mL) was added GO1 (30 mg) and 28% ammonium hydroxide (0.5 mL). The solution was sonicated (Cole Parmer, model 08849-00) for 12 h and then transferred into a Teflon-sealed autoclave. The mixture was hydrothermally heated at 160°C for 12 h. After cooling to r.t., the water was decanted away and the aerogel was rinsed with 15 mL HPLC grade water (2×). The remaining aerogel was freeze-dried by cooling in liquid nitrogen and then sublimating the water under vacuum. Nitrogen doping was performed in a CVD furnace. Typically, the aerogel was placed in a 1-in (2.54 cm) quartz tube. The quartz tube was evacuated to ~ 100 mTorr and filled with Ar/NH_3 (65:65 sccm) to 1 atm. After that, the furnace was raised to 750°C within 30 min and maintained at 750°C for 1 h under contineous Ar/NH_3 flow (65:65 sccm).

2.4. Characterization

TEM was performed using JEOL 2100 field emission gun transmission electron microscope. XPS spectra were taken on a PHI Quantera SXM scanning X-ray microprobe with a base pressure of 5×10^{-8} Torr. A pass energy of 26 eV with a 200 μm beam size was used for elemental spectra. ICP-MS was measured on a Perkin Elmer Nexion 300. The Mn calibration curve is prepared using the Mn standard (Perkin Elmer). The samples were digested in 2% nitric acid (Sigma Aldrich; TraceSELECT Ultra grade) at 50°C for 1 d and filtered over a PTFE membrane with a 0.2 μm pore size. Atomic resolution STEM images were collected with a JEOL-ARM200F operated at 80 kV equipped with a CEOS Cs probe corrector. Collection angles were set to 20–75 mrad for HAADF images and 4.5 mrad for BF images. The convergence angle was set to 24 mrad. EDS analysis was performed with an EDAX Apollo Si detector. The Mn K-edge XAFS spectra were acquired at beamline 1W1B of the Beijing Synchrotron Radiation Facility in fluorescence mode using a fixed-exit Si (111) double crystal monochromator. The X-ray higher harmonics were minimized by detuning the two flat Si (111) crystals to ~ 65% of the maximum incident flux. The incident X-ray beam was monitored by an ionization chamber filled with N_2, and the X-ray fluorescence detection was performed using a Lytle-type detector filled with Ar. The EXAFS raw data were then background-subtracted, normalized and Fourier transformed by the standard procedures with the IFEFFIT package [46].

2.5. Electrochemical Characterization

RDE studies of ORR were conducted in a home-built electrochemical cell using a mercury/mercury oxide electrode (CHI 152, CH Instruments) as the reference electrode and a Pt wire as the counter electrode. The currents were collected using a CHI 608D workstation (CH Instruments). For the preparation of electrodes for ORR testing, catalyst (2 mg) was

dispersed in 0.5 wt% Nafion aqueous solution (2 mL) by sonication (Cole Parmer, model 08849 – 00) until a homogeneous ink was formed. Then 16 μL of the catalyst ink was loaded onto a glassy carbon electrode (5 mm in diameter, Pine Instrument) and dried slowly in air. A flow of O_2 was maintained in the electrolyte during the measurement to ensure continuous O_2 saturation. All of the reference electrodes were calibrated with respect to reversible hydrogen electrode. The calibrations were conducted in high purity hydrogen-saturated electrolyte with a Pt wire as the working electrode at a scan rate of 1 mV s^{-1}. The average of the two potentials of each CV curve where the current crossed zero was taken to be the thermodynamic potential. The mercury/mercury oxide electrode is calibrated as E (RHE) = E (Hg/HgO) + 0.901 V in 0.1 M KOH.

The graphene-based catalysts with different Mn content and ligands were prepared as shown in Fig. 1a. Pristine GO was synthesized using the improved Hummers protocol [29]. Instead of applying the conventional 1× only HCl wash for the purification of GO, we modified the number of acid washes (n) to range from 1 to 6 and the resulting GO products are termed as GOn (n = 1 – 6). After that, the GOn was self-assembled into an aerogel by a hydrothermal reaction in HPLC grade water, and then transformed into NG by annealing in NH_3/Ar at 750°C. The samples so prepared were termed NGn (n = 1 – 6). In a control experiment, we also ran the GO1 hydrothermal reaction in alkaline media (aqueous NH_4OH) to trigger the formation of MnO_x nanoparticles, and then performed the same nitrogen doping. The control sample synthesized in alkaline media was named NG1a.

The Mn content in these samples was characterized using various techniques with different detection limits. No apparent Mn signal was detected in NGn using conventional analytical tools such as XPS or TEM (Fig. 1b–e). As shown in Fig. 1b, only NG1a shows the presence of Mn in the XPS survey spectrum. This is more evident in the high resolution Mn2p XPS spectra corrected according to the C1s peak (Fig. S1a, b). The atomic concentrations of elements are shown in Fig. 1c. All of the NGn have similar compositions of 90% C, 3.5% N, 6.5% O and no detectable Mn. NG1a has 2.5 at% Mn and higher contents of N and O at 6.3 at% and 13 at%, respectively. It is possible that the NGn hydrothermal reaction removed some of the Mn.

3. Discussion

Microscopic imaging can provide direct visual information regarding the surface morphology of the materials. However, due to low resolution and the low contrast of C and Mn atoms, traditional TEM analysis cannot detect the atomic features of metals. As shown in Fig. 1d, the TEM image of NG1 reveals a graphene surface without any apparent nanoparticles. The control NG1a surface clearly contains many nanoparticles with a size distribution of ~ 5 nm (Fig. 1e). In combination with the spectroscopy data and XPS and TEM analyses, the evidence could readily lead to the conclusion that the heteroatom-doped graphene synthesized by this conventional method is metal-free.

However, the evidence for metal-free graphene might be called into question as more sensitive analytical techniques are used. For example, ICP-MS is a highly sensitive instrumental method that detects metals at the ppm or lower concentration [31]. As shown in

Fig. 2a, the Mn signal in NGn emerges and its content decreases rapidly as the number of acid washes increase. The Mn contents are ~560, 360, 32 and 13 ppm in NG1, NG2, NG3 and NG4, respectively; and Mn is not detectable in NG5 and NG6. Energy dispersive X-ray spectra (EDS) taken on the scanning transmission electron microscopy (STEM) images also have results consistent with the ICP-MS in that there is a Mn peak at 5.9 keV for NG1 but the signal disappears for NG6 (Fig. 2b and Fig. S2).

To unravel the structural information of Mn in NGn, we first employed HAADF-STEM analysis, which offers higher contrast between metallic and non-metallic atoms due to their different scattering behaviors. Fig. 2c–f and S3 show the HAADF-STEM images of NGn, in which the Mn atoms appear as bright spots and are clearly distinguishable from the dark carbon background [25]. As shown in Fig. 2c and Fig. S3a–b, NG1 contains a large amount of Mn on the graphene surface that is distributed as single atoms or in few-atom clusters. For NG2 (Fig. 2d and S3c–d), the abundance of clustered atoms decreases greatly and the Mn primarily exists as single atoms. This atomic feature is also present in NG3 and NG4, yet in a much lower abundance (Fig. 2e and Fig. S3e–h). However, the Mn signal becomes barely detectable for NG6 (Fig. 2f and Fig. S3i).

To better understand the Mn atomic environment, NGn and NG1a were further investigated using XANES and EXAFS. For lack of sufficient signals for NG3-6, their spectra are not shown. From Fig. 3a, it can be observed that the XANES spectra of NG1 and NG2 are drastically distinctive from those of bulk Mn, MnO and MnO_2. The XANES absorption edges of NG1 and NG2 lie between MnO and MnO2 references, which suggests the valences of Mn are between +2 and +4. However, the XANES spectrum of NG1a shows an overall profile similar to that of the MnO_2 reference, with a slightly shifted absorption edge to higher energy as compared to NG1 and NG2 and thus higher valence, indicating that the Mn species can be dominated by nanocrystalline MnO_2. The existing forms of Mn are further elucidated from the Fourier transforms (FT) of the experimental Mn K-edge EXAFS spectra (Fig. 3b). The NG1, NG2 and NG1a exhibit a main peak at 1.47 Å, which nearly coincides with the first Mn-O peak of the MnO_2 reference and hence can be attributed to the light atom contribution. Another peak is revealed at ~ 2.35 Å, which overlaps with the Mn-Mn peaks for bulk Mn and MnO_2 references that spread from 2.32 to 2.52 Å and can be assigned to the Mn-Mn scattering. This peak intensity is much weaker for NG2 and shows an obvious increase for NG1, which is in agreement with the observation of few-atom clusters in NG1 and fewer clustering features in NG2 under HAADF-STEM. The coordination configurations for the Mn atoms are then investigated by quantitative least-squares EXAFS curve fitting analysis (Fig. S4 and Supplementary Table S1). For NG2, in addition to the minor Mn-Mn bond having a coordination number of 0.2 at a distance of 2.51 Å, it is rather surprising that two different nearest-neighbor coordination spheres from light atoms are estimated to be at distances of 1.94 and 2.23 Å with coordination numbers of 3.0 and 1.9, respectively (Supplementary Table S1). Despite an obvious increase of Mn-Mn coordination degree, similar bond-distance distribution is shown in NG1. Those results are in marked contrast to the porphyrin-, the pyridine- and the graphene-divacancy-based motifs previously reported in the literature, where more distant coordination spheres of C atoms around the metal atoms were usually found at distances of beyond 2.7 Å, with the first coordination spheres of N atoms at ~ 2.0 Å [26,32]. These results are confirmed by a
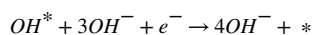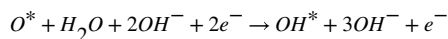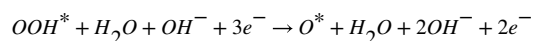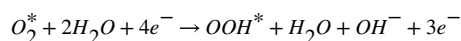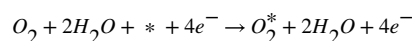
comparison of the experimental XANES spectra of NG1 and NG2 with the theoretical spectra for the MnN_xC_y moieties built based on the three archetypical architectures (Fig. S5), where the features for the experimental XANES spectra are only partially reproduced. The deviations of NG1 and NG2 from the perfect crystalline archetypical architectures are in accord with the amorphous nature of graphene oxide produced by the improved Hummer's method. Furthermore, density functional theory (DFT) calculations reveal that two or more different bond-distance distributions for the nearest Mn-C/N/O bonding can be observed in the four-vacancy-based moiety in the graphene (Fig. S5). Those results suggest that the majority of Mn atoms in NG1 and NG2 are dispersed in the largely defective graphene sheet as mononuclear centers without definite uniform coordination configurations.

The catalytic activities of different structures on NG were evaluated in O_2-saturated 0.1 M KOH solution using a rotating-disk electrode (RDE, Fig. 4). Fig. 4a,b and Fig. S6 display the linear sweep voltammetry (LSV) of NGn under different rotating speeds. The electron transfer numbers extrapolated from the linear fitting of the Koutechy-Levich plots (insets of their corresponding LSV) at the selected potentials are summarized in Fig. 4d [5,33]. For NG1, where single atoms and few-atom clusters are present, the number of electrons in the ORR is ~3.9. The electron process reaches its maximum at 4.0 for NG2, in which the Mn mononuclear-centered architecture dominates, and then deceases to ~ 3.0 for NG3 and NG4, in which the abundance of mononuclear features decreases. For NG6, which represents the essentially metal-free NG structure, the number of electrons is only ~2.5, which indicates the oxygen is mainly reduced to peroxide. For the nanostructure MnO_x in NG1, oxygen is reduced by a 3.1 electron process with an onset potential of 0.8 V. The performance of NG1a lies between the reported values of MnO_x from 1.7 to 3.9 electrons with onset potentials ranging from 0.75 to 0.90 V, which are dependent on the crystallinity and structural composition [13,34–35]. The ORR catalytic activity of NGn and NG1a are further analyzed by comparing their LSV at 1225 rpm (Fig. 4e) and the result is summarized in Fig. 4f. The onset potentials for NG2, NG6 and NG1a are 0.94, 0.73 and 0.83 V, respectively. This suggests that the mononuclear structure requires less energy for the initiation of ORR than those of NG and nanostructured MnO_x. Both NG1 and NG2 exhibit a much higher current density at 0.6 V vs RHE. The current densities at 0.6 V and half-wave potential ($E_{1/2}$) decrease gradually from NG2 to NG6, which correlates with the Mn concentrations determined by ICP-MS (Fig. 2a). There are factors that can contribute to the electrocatalytic activity difference across the literature: (a) in the literature, the LSV is measured at 1600 rpm in some cases. Here we use 1225 rpm to avoid the separation of the catalysts from the electrode and therefore ensure higher reproducibility. Increasing the rotating speed will enhance the mass transport and increase the current density at the diffusion limited current. (b) The catalyst loadings could be different. This includes two components, one is the total amount of catalyst, the other is the trace metal. For the latter, it is difficult to correlate the literature results due to the differing amounts of residual metal in GO prepared by different laboratories.

Since the ORR activity of NG is associated with the Mn content and its structure, this information provides an approach for the engineering of NG into a better-performing ORR catalyst. For example, the addition of 2.5 μmol $MnCl_2$ to 30 mg GO6 during the hydrothermal reaction leads to an enhanced ORR performance. As shown in Fig. S7, the

number of electrons in ORR improves from 2.5 for NG6 to 4, and the current density at 0.4 V increases from −1.4 mA cm^{-2} to −3.2 mA cm^{-2}. Both the current density and the number of electrons in ORR for NG6 can be recovered to a performance similar to that of NG2 after the introduction of trace Mn, yet the onset overpotential remains to be further optimized. Nonetheless, it underscores the profound effect of the trace Mn on the electrochemical reaction.

To understand the mechanism of these ORR catalytic behaviors, spin-polarized density DFT calculations were performed using Vienna *ab-initio* Simulation Package (VASP) [36] code (see Supplementary data for details). ORR catalytic activities on four types of samples, graphene, NG, Mn mononuclear-centered NG, and MnO_2 crystal surface, were taken into consideration. In alkaline solution ORR follows the associative rather than the dissociative mechanism as steps [36–39]:

$$O_2 + 2H_2O + \, * \, + 4e^- \rightarrow O_2^* + 2H_2O + 4e^-$$

$$O_2^* + 2H_2O + 4e^- \rightarrow OOH^* + H_2O + OH^- + 3e^-$$

$$OOH^* + H_2O + OH^- + 3e^- \rightarrow O^* + H_2O + 2OH^- + 2e^-$$

$$O^* + H_2O + 2OH^- + 2e^- \rightarrow OH^* + 3OH^- + e^-$$

$$OH^* + 3OH^- + e^- \rightarrow 4OH^- + \, *$$

The Gibbs free energy diagrams of the ORR intermediates bound on different samples under the conditions of pH 14 are shown in Fig. 5. According to the Sabatier principle, a good catalyst should bind a key intermediate in a manner that it is strong enough to allow the reagents to stay on samples for reaction but weak enough to enable the release of products. The Gibbs free energy diagram indicates that the intermediates are bound so weakly on graphene that the highest barrier is 1.37 eV. The structure of Mn mononuclear-centered NG is established based on the previous XANES and EXAFS study, with variations on the surrounding binding elements. It has been reported that Mn-oxo (Mn = O) species are active in various catalytic reactions [41–42], thus 3 relaxed Mn-oxo (Mn = O) species were proposed as the initial states for ORR, and shown in Fig. 5b–d. The structure is formulated as Mn-oxo-N_xO_y, where x and y indicate the number of nitrogen and oxygen atoms coordinated to the Mn center. The Gibbs free energy diagrams show that these Mn-oxo species exhibit stronger adsorption ability of ORR intermediates than graphene, resulting in significant decrease of the reaction barriers. The rate-determining step barriers are 0.84 eV, 0.52 eV and 0.68 eV for Mn-oxo-N_2O_2, Mn-oxo-N_3O_1 and Mn-oxo-N_4, respectively,

implying that they are much more active for ORR catalysis. For comparison, the structure of NG was generated from Mn-oxo-N_4 with Mn = O removed, and after relaxation it reconstructed as shown in Fig. 5e. From the view of the Gibbs free energy diagram, NG also has stronger adsorption ability of ORR intermediates than does graphene, but its rate-determining step barrier is still high at 1.57 eV. For the case of the MnO_2 crystal surface, we focused on the stable and preferentially exposed β-MnO_2 crystal (110) surface. It has been well established that in alkaline media the most thermodynamically stable state of this surface is full coverage with splitting H_2O [43–44], and we took the most stable state as the initiation of ORR, as in Fig. S8f. The Gibbs free energy diagram shows the weak binding of ORR intermediates on the β-MnO_2 crystal (110) surface, and the highest barrier is 1.32 eV. All the ORR intermediates adsorption structures on four types of samples are provided in Fig. S8a–e,g. These DFT results illustrate that the Mn mononuclear-centered NG architectures significantly enhances the ORR performance of graphene.

4. Conclusion

In summary, we have prepared graphene-based catalysts with different structures and determined their catalytic ORR activities with and without trace Mn. This study shows the deceptive nature of trace metal that resides below the detection limit of XPS and common TEM analysis. This leads to a misinterpretation of mechanisms in graphene-based catalysts. It is further found that the Mn mononuclear-centered structures within graphene have a higher ORR activity than those of metal-free NG and MnO_x nanoparticles. This discovery shows the important role of trace metal in the electrochemical performance of graphene materials, and it provides a method for further optimization of graphene-based ORR catalysts. More specifically, a balance is needed between the increase of Mn-centered active sites and the aggregation of Mn metal. Moreover, it has implications for development of other catalysts by tuning the coordination chemistry on the graphene. By exploiting the high conductivity and excellent stability of graphene [7–8], mimicry of enzymes such as hydrogenase and oxygenase, where the mono- or bi-nuclear metal center acts as the active site [45–46], is possible. This holds great promise for graphene materials to be electrocatalysts in a broad array of applications.

Supplementary Material

Refer to Web version on PubMed Central for supplementary material.

Acknowledgments

References

1. Xiang CS, Cox PJ, Kukovecz A, Genorio B, Hashim DP, Yan Z, et al. Functionalized low defect graphene nanoribbons and polyurethane composite film for improved gas barrier and mechanical performances. ACS Nano. 2013; 7:10380–10386. [PubMed: 24102568]

2. Kim HW, Yoon HW, Yoon SM, Yoo BM, Ahn BK, Cho YH, et al. Selective gas transport through few-layered graphene and graphene oxide membranes. Science. 2013; 342:91–95. [PubMed: 24092738]

3. Torrisi F, Hasan T, Wu WP, Sun ZP, Lombardo A, Kulmala TS, et al. Inkjet-printed graphene electronics. ACS Nano. 2012; 6:2992–3006. [PubMed: 22449258]

4. Ye R, Liu L, Peng Z, Wang T, Jalilov AS, Yakobson BI, et al. High performance electrocatalytic reaction of hydrogen and oxygen on ruthenium nanoclusters, ACS Appl. Mater Interfaces. 2017; 9:3785–3791.

5. Ye RQ, Peng ZW, Wang T, Xu YN, Zhang JB, Li YL, et al. In situ formation of metal oxide nanocrystals embedded in laser-induced graphene. ACS Nano. 2015; 9:9244–9251. [PubMed: 26284900]

6. Bolotin KI, Sikes KJ, Jiang Z, Klima M, Fudenberg G, Hone J, et al. Ultrahigh electron mobility in suspended graphene. Solid State Commun. 2008; 146:351–355.

7. Wu ZS, Ren W, Gao L, Zhao J, Chen Z, Liu B, et al. Synthesis of graphene sheets with high electrical conductivity and good thermal stability by hydrogen arc discharge exfoliation. ACS Nano. 2009; 3:411–417. [PubMed: 19236079]

8. Lee C, Wei X, Kysar JW, Hone J. Measurement of the elastic properties and intrinsic strength of monolayer graphene. Science. 2008; 321:385–388. [PubMed: 18635798]

9. Fei HL, Ye RQ, Ye GL, Gong YJ, Peng ZW, Fan XJ, et al. Boron- and nitrogen- doped graphene quantum dots/graphene hybrid nanoplatelets as efficient electrocatalysts for oxygen reduction. ACS Nano. 2014; 8:10837–10843. [PubMed: 25251218]

10. Qu LT, Liu Y, Baek JB, Dai LM. Nitrogen-doped graphene as efficient metal-free electrocatalyst for oxygen reduction in fuel cells. ACS Nano. 2010; 4:1321–1326. [PubMed: 20155972]

11. Farzaneh A, Saghatoleslami N, Goharshadi EK, Gharibi H, Ahmadzadeh H. 3-D mesoporous nitrogen-doped reduced graphene oxide as an efficient metal-free electrocatalyst for oxygen reduction reaction in alkaline fuel cells: Role of pi and lone pair electrons. Electrochim Acta. 2016; 222:608–618.

12. Geng DS, Chen Y, Chen YG, Li YL, Li RY, Sun XL, et al. High oxygen-reduction activity and durability of nitrogen-doped graphene. Energy Environ Sci. 2011; 4:760–764.

13. Tan YM, Xu CF, Chen GX, Fang XL, Zheng NF, Xie QJ. Facile synthesis of manganese-oxide-containing mesoporous nitrogen-doped carbon for efficient oxygen reduction. Adv Funct Mater. 2012; 22:4584–4591.

14. Li YG, Zhou W, Wang HL, Xie LM, Liang YY, Wei F, et al. An oxygen reduction electrocatalyst based on carbon nanotube-graphene complexes. Nat Nanotechnol. 2012; 7:394–400. [PubMed: 22635099]

15. Liang J, Jiao Y, Jaroniec M, Qiao SZ. Sulfur and nitrogen dual-doped mesoporous graphene electrocatalyst for oxygen reduction with synergistically enhanced performance. Angew Chem Int Ed. 2012; 51:11496–11500.

16. Masa J, Xia W, Muhler M, Schuhmann W. On the role of metals in nitrogen-doped carbon electrocatalysts for oxygen reduction. Angew Chem Int Ed. 2015; 54:10102–10120.

17. Wang L, Ambrosi A, Pumera M. "Metal-free" catalytic oxygen reduction reaction on heteroatom-doped graphene is caused by trace metal impurities. Angew Chem Int Ed. 2013; 52:13818–13821.

18. Panich AM, Shames AI, Aleksenskii AE, Dideikin A. Magnetic resonance evidence of manganese-graphene complexes in reduced graphene oxide. Solid State Commun. 2012; 152:466–468.

19. Ambrosi A, Chua CK, Khezri B, Sofer Z, Webster RD, Pumera M. Chemically reduced graphene contains inherent metallic impurities present in parent natural and synthetic graphite. Proc Natl Acad Sci U S A. 2012; 109:12899–12904. [PubMed: 22826262]

20. Wong CHA, Sofer Z, Kubesova M, Kucera J, Matejkova S, Pumera M. Synthetic routes contaminate graphene materials with a whole spectrum of unanticipated metallic elements. Proc Natl Acad Sci U S A. 2014; 111:13774–13779. [PubMed: 25201990]

21. Chua CK, Ambrosi A, Sofer Z, Mackova A, Havranek V, Tomandl I, et al. Chemical preparation of graphene materials results in extensive unintentional doping with heteroatoms and metals. Chem Eur J. 2014; 20:15760–15767. [PubMed: 25284355]

22. Ambrosi A, Chee SY, Khezri B, Webster RD, Sofer Z, Pumera M. Metallic impurities in graphenes prepared from graphite can dramatically influence their properties. Angew Chem Int Ed. 2012; 51:500–503.

23. Yao SY, Zhang X, Zhou W, Gao R, Xu WQ, Ye YF, et al. Atomic-layered Au clusters on alpha-MoC as catalysts for the low-temperature water-gas shift reaction. Science. 2017; 357:389–393. [PubMed: 28642235]

24. Zhao JX, Chen ZF. Single mo atom supported on defective boron nitride monolayer as an efficient electrocatalyst for nitrogen fixation: A computational study. J Am Chem Soc. 2017; 139:12480–12487. [PubMed: 28800702]

25. Fei H, Dong J, Arellano-Jimenez MJ, Ye G, Kim ND, Samuel ELG, et al. Atomic cobalt on nitrogen-doped graphene for hydrogen generation. Nat Commun. 2015; 6

26. Deng D, Chen X, Yu L, Wu X, Liu Q, Liu Y, et al. A single iron site confined in a graphene matrix for the catalytic oxidation of benzene at room temperature. Sci Adv. 2015; 1:e1500462. [PubMed: 26665170]

27. Wu JJ, Liu MJ, Sharma PP, Yadav RM, Ma LL, Yang YC, et al. Incorporation of nitrogen defects for efficient reduction of CO_2 via two-electron pathway on three-dimensional graphene foam. Nano Lett. 2016; 16:466–470. [PubMed: 26651056]

28. Song Y, Peng R, Hensley DK, Bonnesen PV, Liang LB, Wu ZL, et al. High-selectivity electrochemical conversion of CO_2 to ethanol using a copper nanoparticle/N-doped graphene electrode. Chemistryselect. 2016; 1:6055–6061.

29. Marcano DC, Kosynkin DV, Berlin JM, Sinitskii A, Sun Z, Slesarev A, et al. Improved synthesis of graphene oxide. ACS Nano. 2010; 4:4806–4814. [PubMed: 20731455]

30. Newville M. IFEFFIT: Interactive XAFS analysis and FEFF fitting. J Synchrotron Radiat. 2001; 8:322–324. [PubMed: 11512767]

31. Jenner GA, Longerich HP, Jackson SE, Fryer BJ. ICP-MS - a powerful tool for high-precision trace-element analysis in earth sciences - evidence from analysis of selected usgs reference samples. Chem Geol. 1990; 83:133–148.

32. Liu WG, Zhang LL, Yan WS, Liu XY, Yang XF, Miao S, et al. Single-atom dispersed Co-N-C catalyst: structure identification and performance for hydrogenative coupling of nitroarenes. Chemical Science. 2016; 7:5758–5764. [PubMed: 30034714]

33. Liang Y, Li Y, Wang H, Zhou J, Wang J, Regier T, et al. Co_3O_4 nanocrystals on graphene as a synergistic catalyst for oxygen reduction reaction. Nat Mater. 2011; 10:780–786. [PubMed: 21822263]

34. Meng YT, Song WQ, Huang H, Ren Z, Chen SY, Suib SL. Structure-property relationship of bifunctional MnO_2 nanostructures: Highly efficient, ultra-stable electrochemical water oxidation and oxygen reduction reaction catalysts identified in alkaline media. J Am Chem Soc. 2014; 136:11452–11464. [PubMed: 25058174]

35. Lima FHB, Calegaro ML, Ticianelli EA. Investigations of the catalytic properties of manganese oxides for the oxygen reduction reaction in alkaline media. J Electroanal Chem. 2006; 590:152–160.

36. Kresse G, Furthmüller J. Efficient iterative schemes for ab initio total-energy calculations using a plane-wave basis set. Phys Rev B. 1996; 54:11169–11186.

37. Nørskov JK, Rossmeisl J, Logadottir A, Lindqvist L, Kitchin JR, Bligaard T, et al. Origin of the overpotential for oxygen reduction at a fuel-cell cathode. J Phys Chem B. 2004; 108:17886–17892.

38. Yu L, Pan X, Cao X, Hu P, Bao X. Oxygen reduction reaction mechanism on nitrogen-doped graphene: A density functional theory study. J Catal. 2011; 282:183–190.

39. Gong Y, Fei H, Zou X, Zhou W, Yang S, Ye G, et al. Boron- and nitrogen-substituted graphene nanoribbons as efficient catalysts for oxygen reduction reaction. Chem Mater. 2015; 27:1181–1186.

40. Zhang C, Sha J, Fei H, Liu M, Yazdi S, Zhang J, et al. Single-atomic ruthenium catalytic sites on nitrogen-doped graphene for oxygen reduction reaction in acidic medium. ACS Nano. 2017

41. Massie AA, Denler MC, Cardoso LT, Walker AN, Hossain MK, Day VW, et al. Equatorial ligand perturbations influence the reactivity of manganese(IV)-oxo complexes. Angew Chem Int Ed. 2017; 56:4178–4182.

42. Ogliaro F, de Visser SP, Groves JT, Shaik S. Chameleon states: High-valent metaL-oxo species of cytochrome P450 and its ruthenium analogue. Angew Chem Int Ed. 2001; 40:2874–2878.

43. Cheng F, Zhang T, Zhang Y, Du J, Han X, Chen J. Enhancing electrocatalytic oxygen reduction on MnO_2 with vacancies. Angew Chem Int Ed. 2013; 52:2474–2477.

44. Zhang B, Liu J, Yang Y, Chang M. Oxidation mechanism of elemental mercury by HCl over MnO_2 catalyst: Insights from first principles. Chem Eng J. 2015; 280:354–362.

45. Berggren G, Adamska A, Lambertz C, Simmons TR, Esselborn J, Atta M, et al. Fontecave, Biomimetic assembly and activation of [FeFe]-hydrogenases. Nature. 2013; 499:66–69. [PubMed: 23803769]

46. Schuller DJ, Wilks A, de Montellano PRO, Poulos TL. Crystal structure of human heme oxygenase-l. Nat Struct Biol. 1999; 6:860–867. [PubMed: 10467099]
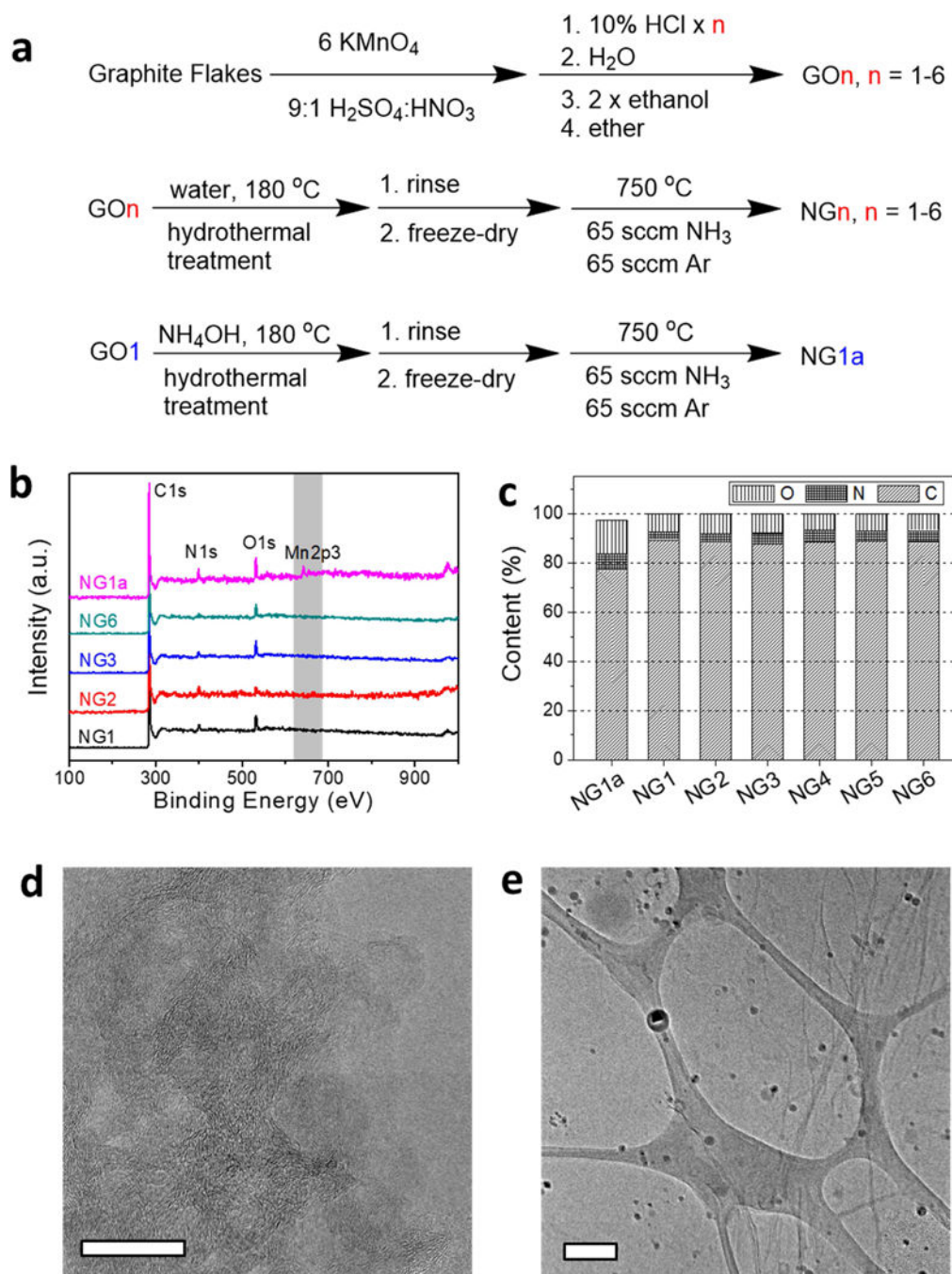
Fig. 1.
Synthesis of materials and characterization by XPS and TEM. (a) Reaction scheme for the synthesis of NGn and NG1a. (b) XPS survey spectra of NGn and NG1a. (c) Atomic concentrations of C, N, O determined by XPS. No apparent Mn signal is detected by XPS in NGn, (n = 1-6). The Mn content in NG1a is ~ 2.5 at%. (d) TEM image of NG1 with no apparent nanoparticles on the graphene surface. The scale bar is 20 nm. (e) TEM image of NG1a on a lacey carbon grid with ~5 nm diameter nanoparticles distributed on graphene. The scale bar is 200 nm.
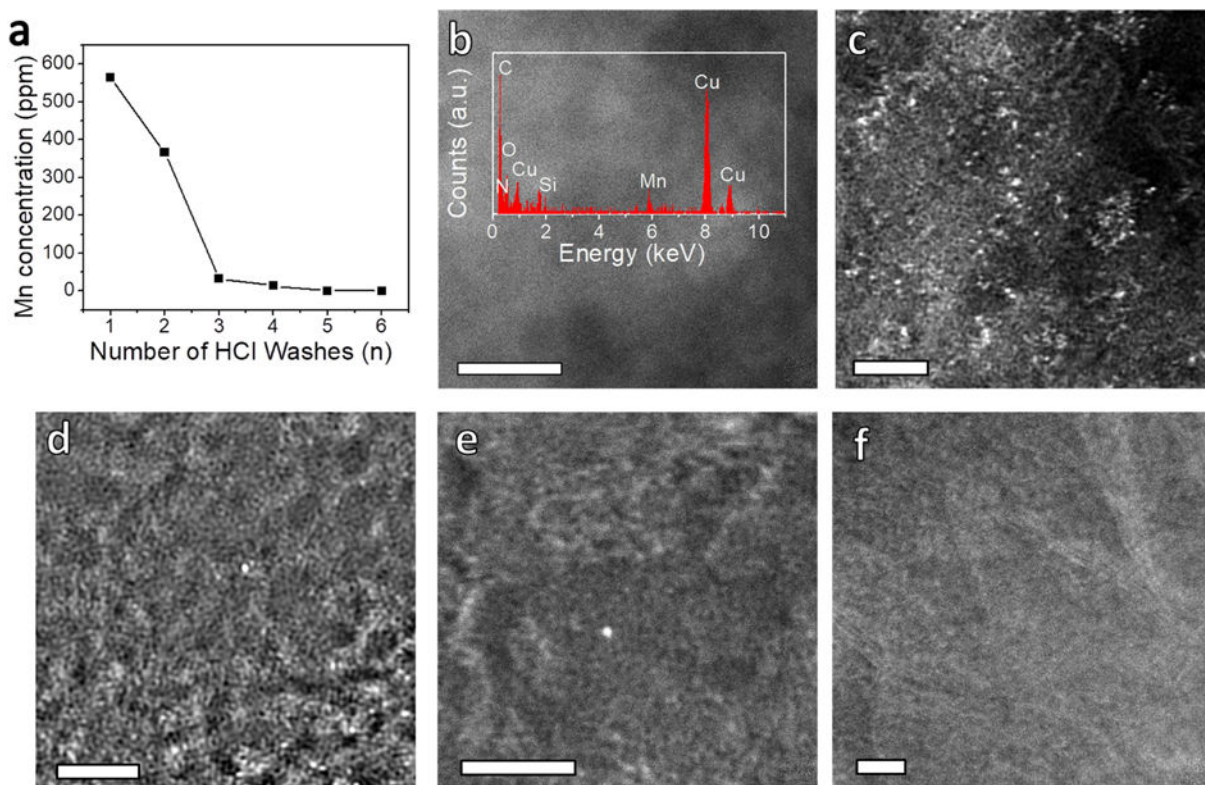
Fig. 2.
Mn detection on graphene using enhanced sensitivity techniques. (a) Concentrations of Mn in NGn, (n = 1-6) determined by ICP-MS. (b) STEM image of NG1. Inset is the EDS showing the presence of Mn. The scale bar is 5 nm. HAADF-STEM images of (c) NG1, (d) NG2, (e) NG3 and (f) NG6. The scale bars are 2 nm in (c)-(f).
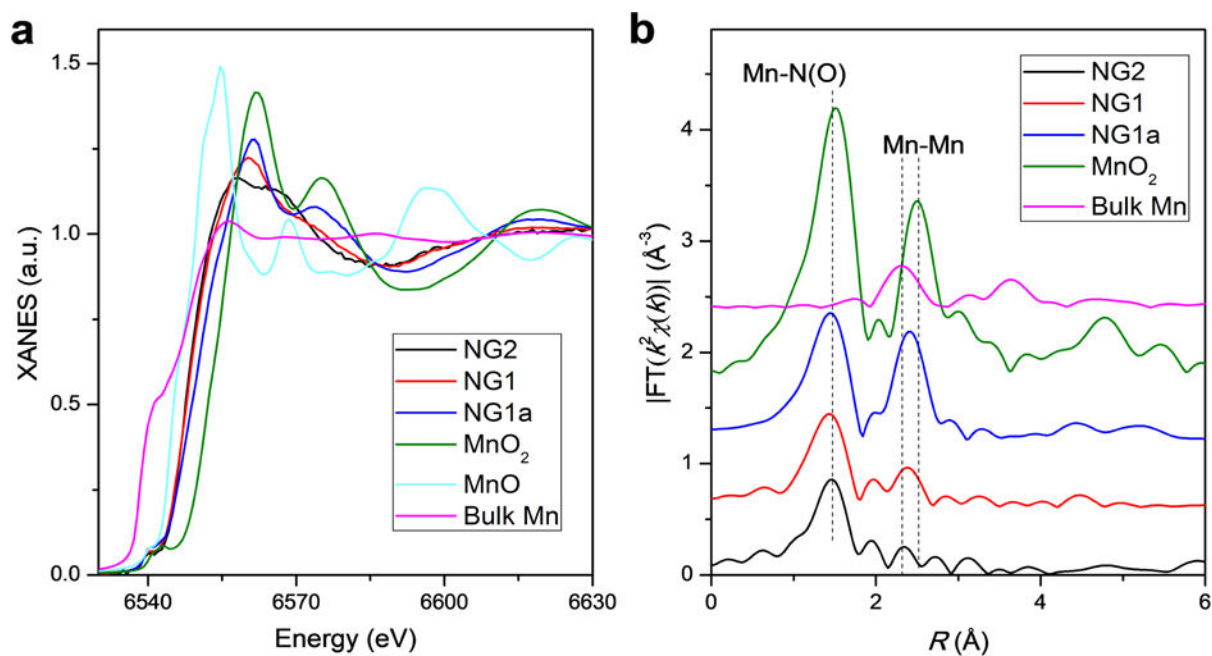
Fig. 3.
Local structure characterization of Mn in NGn and NG1a. (a) Experimental Mn K-edge
XANES spectra of NG1, NG2, NG1a and the standard references (bulk Mn, MnO and
MnO_2). No Mn signal is detected in NG 3-6. (b) Fourier transformed magnitudes of the
experimental Mn K-edge EXAFS spectra for NG1, NG2, NG1a and the standard references
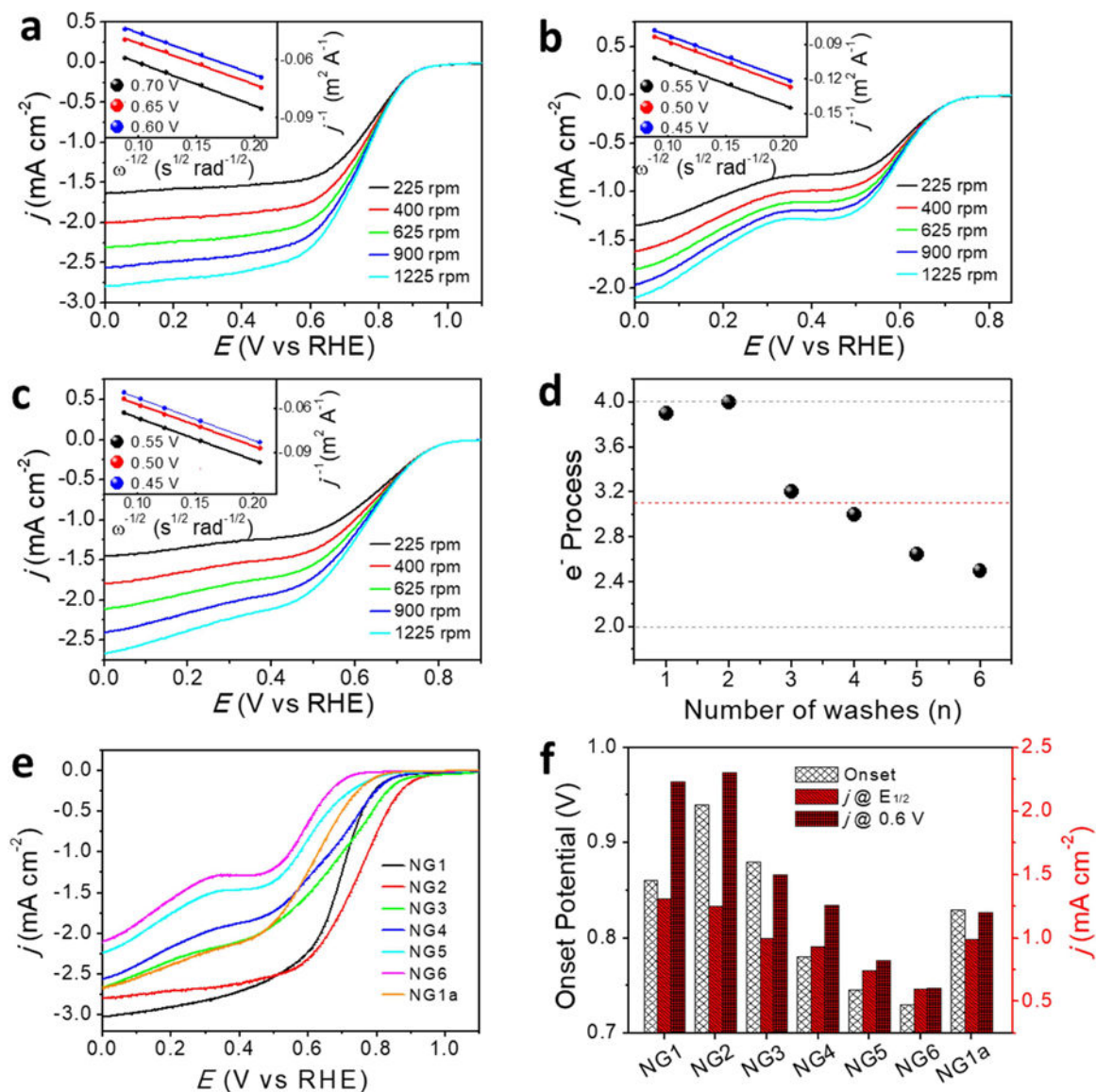(bulk Mn and MnO_2).

Fig. 4.
ORR activity of NGn and NG1a. Rotating-disk voltammograms of (a) NG2, (b) NG6, (c)
NG1a in O$_2$-saturated 0.1 M KOH at a scan rate of 5 mV s^{-1}. Inset shows the corresponding
Koutechy-Levich plots at different potentials. (d) Summary of the electron number process
for ORR at indicated potential calculated from their Koutechy-Levich plots. The red dashed
line is the NG1a sample, and the grey dashed lines indicate the full (4 e$^-$) and half (2 e$^-$)
oxygen reduction. (e) Linear sweep voltammetries of NGn and NG1a at 1225 rpm in O$_2$-
saturated 0.1 M KOH at a scan rate of 5 mV s^{-1}. (f) Comparison of ORR activities of NGn
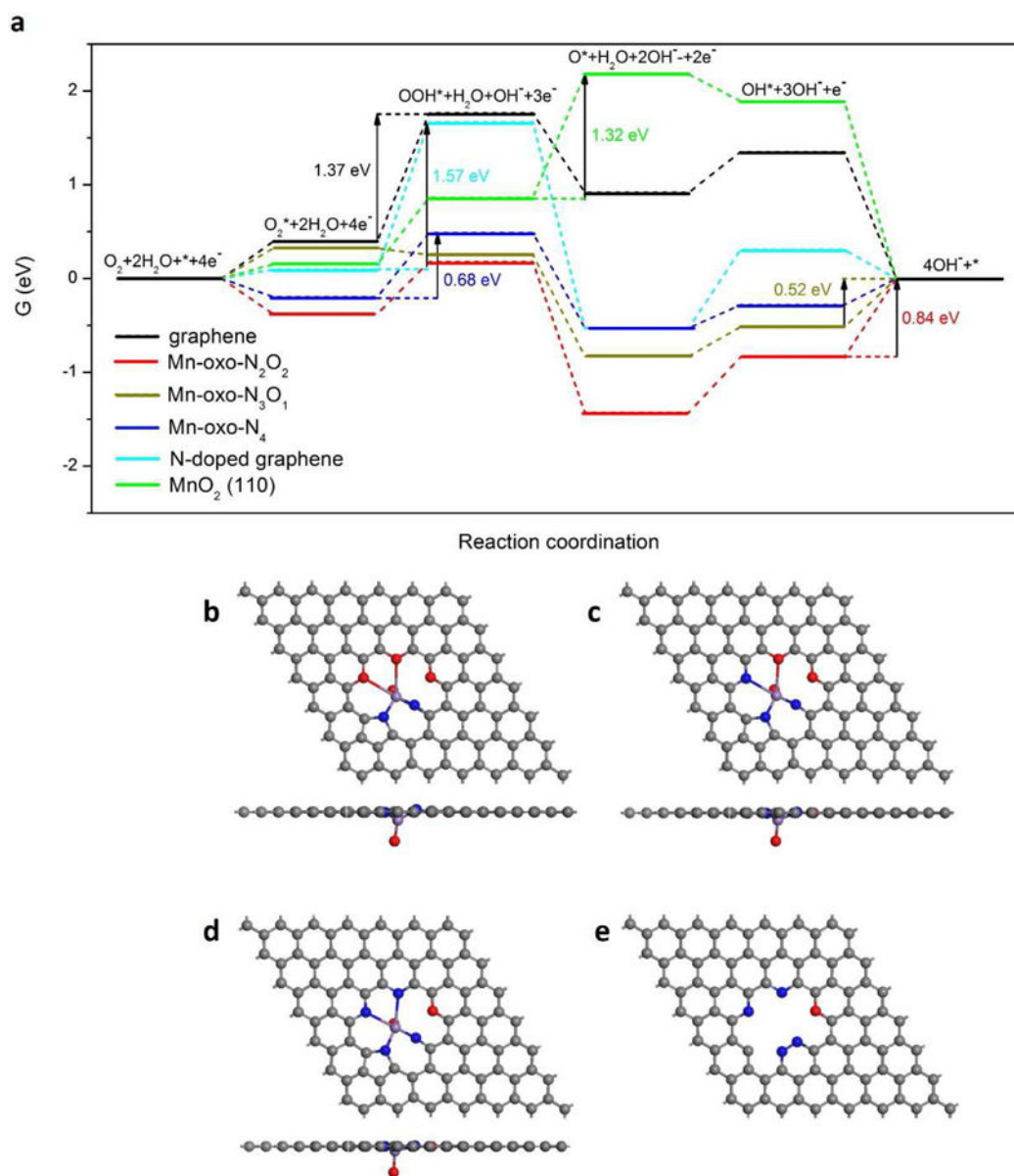and NG1a.

Fig. 5.
ORR activities predicted by DFT simulation. (a) Gibbs free energy diagram for ORR on different samples under conditions of pH 14 and the maximum potential allowed by thermodynamics. Atomic structures of (b) $Mn-oxo-N_2O_2$, (c) $Mn-oxo-N_3O_2$, (d) $Mn-oxo-N_4$ and (e) NG. Grey, blue and red balls represent C, N and O elements, respectively.